– Supporting Information –

Stability of Ultra-Thin Ceria Films on Pt(111) Exposed to Air and Treated in Redox Cycles

G. Gasperi,[†] P. Luches,[†] and C. Barth*[,‡]

Istituto Nanoscienze, Consiglio Nazionale delle Ricerche, Via G. Campi 213/a, Modena 41125, Italy, and Aix-Marseille Université, CNRS, CINaM UMR 7325, 13288 Marseille, France

E-mail: barth@cinam.univ-mrs.fr

*To whom correspondence should be addressed

[†]Istituto Nanoscienze, Consiglio Nazionale delle Ricerche, Via G. Campi 213/a, Modena 41125, Italy

[‡]Aix-Marseille Université, CNRS, CINaM UMR 7325, 13288 Marseille, France

1 PREPARATION OF SURFACES

Surface preparation (Modena) - The film preparation was done at the CNR NANO laboratory in Modena (Italy). The Pt(111) substrate (Surface Preparation Laboratory, Zaandam, The Netherlands) was cleaned by repeated cycles of sputtering (1 keV, 1 μA) and annealing (770 °C) in ultra-high vacuum (UHV). After the cleaning procedure, the substrate showed flat terraces hundreds of nanometers wide and low energy electron diffraction (LEED) showed a sharp (111) pattern. The concentration of impurities on the sample surface was below the photoemission X-ray spectroscopy (XPS) detection limit.

A cerium oxide (ceria) ultra-thin film was grown by reactive evaporation of ultra-pure cerium: cerium pieces were cut from larger lumps (3N purity, MaTeck, Jülich, Germany) and annealed in a molybdenum bottle-like crucible that is placed in an e-beam evaporator (EV40, Ferrovac GmbH, Switzerland). The evaporation rate was approximately 0.2 Å/min, measured by a quartz microbalance (XTC controller, INFICON, Switzerland). For this study, a film with a nominal 2.3 monolayer (ML) thickness was used. During the evaporation, molecular oxygen (5.5N, Air Liquide, Paris, France) was supplied through a nozzle such that a background O_2 pressure of 1×10^{-7} mbar was reached. The Pt(111) substrate was kept at room temperature (RT) during the evaporation. After the growth, the cerium oxide film was annealed at 770 °C in 1×10^{-7} mbar O_2 pressure for 15 min to obtain an epitaxial film with large flat terraces and to fully oxidize the film with a low Ce^{3+} concentration[1].

Sample transfer - After STM and XPS experiments had been conducted at the CNR Nano laboratory in Modena, the sample was extracted from the UHV and quickly put into a glas vacuum desiccator, which was then filled with atmospheric nitrogen. A time of ∼5 minutes was needed for the sample transfer in air and the filling of the desiccator with nitrogen. The sample was then carried to the CINaM laboratory in Marseille (France), where the ceria sample was removed from the desiccator and quickly transferred into the load-lock part of the UHV system. Again a time of ∼5 minutes was needed for the sample transfer in air, from the desiccator to the UHV chamber, including the time needed for the starting of the pumping.

Sample treatments (Marseille) - For the *reduction of the ceria sample* by UHV annealing, the sample was quickly placed inside a hot oven, which is located inside the UHV system[2]. At high temperatures, the sample reached the same temperature as the UHV oven after about 7 minutes. When the sample was post-annealed at, e.g., ∼650 °C the residual gas pressure did not exceed a value of 7×10^{-10} mbar after an hour of annealing. For the *oxidation of the ceria sample*, the UHV chamber was first back-filled with molecular oxygen (Oxygen 4.5, Linde MINICAN, Munich, Germany) via a leakage valve while constantly monitoring the pressure. An oxygen pressure of 1.0 to 5.0×10^{-7} mbar was used. With the UHV oven kept at a given temperature and the ceria sample at RT, the sample was quickly placed inside the hot oven. After 7 minutes,

Table S1: The different preparation steps taken on the Pt(111) supported 2.3 ML ultra-thin ceria film, which was used for the entire work. The parameters n_C, p, T and t denote the cycle number, pressure (10^{-9} mbar), temperature (°C) and preparation time (min). The last column lists the figures of STM and nc-AFM measurements, which were conducted after the respective preparation step.

Lab	Prep. step	n_C	p	T	t	Images
Modena	Growth	/	< 0.5	RT	7	
Modena	Oxidation	/	100	770	15	Figure 1a
Marseille	Oxidation1	1	500	666	15	Figure 1c
Marseille	Oxidation2	1	500	666	15	Figure 3b
Marseille	Reduction 1	1	< 2.0	639	100	Figure 3c
Marseille	Reduction2	1	< 2.0	700	60	Figure S2
Marseille	Reduction3	1	< 0.5	580	480	Figure 3d
Marseille	Oxidation1	2	500	600	60	Figure 3e
						Figure 5a,b
Marseille	Reduction 1	2	< 1.0	639	100	Figure 3f
						Figure 5c,d
Marseille	Oxidation 1	/	100	636	10	/
Modena	Oxidation	/	100	650	15	
Modena	Reduction	/	< 0.5	630	100	

the sample reached the same temperature as the UHV oven. Typical annealing times were between 10 and 60 minutes. After the oxygen exposure, the sample was immediately extracted from the oven to avoid further reactions at high temperatures. In the first 2 seconds, the temperature decreased from $\sim$650 °C by some hundreds of degrees and within a minute onto an estimated temperature of $<$ 200 °C. After the latter low temperature had been reached, the oxygen supply was closed. Table S1 lists all preparation steps that were done in the two laboratories.

2 EXPERIMENTAL TECHNIQUES

STM and LEED experiments were conducted at both laboratories in UHV and at RT, with the instruments being almost identical. XPS was done only in Modena whereas nc-AFM and KPFM were only done in Marseille.

SPM (NANO, CINaM) - In each of the two laboratories, the same type of RT Omicron AFM/STM (Scienta Omicron, Taunusstein, Germany) was used. The AFM/STM in Marseille is equipped with the SCALA electronics (Scienta Omicron, Taunusstein, Germany), which is controlled by the SCALA 4.1 and

IDL 5.1 software running under SUN Solaris 2.5 on a SUN UNIX derivative. The graphical output of the SUN is sent to a Lubuntu[3] GNU/Linux computer to increase the speed of the SCALA graphics[4]. At the NANO the acquisition system runs under Windows NT and is used in its original configuration.

At both places, the sample surface was imaged for at least half an hour, after the coarse approach of the surface to the SPM tip without recording any image. After this time, most of the drift of the scanner was reduced and maximum stability was reached. All SPM images were analyzed and prepared with the Gwyddion software[5], whereas the colormaps from Matplotlib[6] under Python[7] were used for the 3D color space of the images.

STM (NANO, CINaM) - The STM images were acquired in the constant current mode. The bias voltage was applied to the sample whereas the tip was at ground. STM experiments were conducted with electrochemically etched tungsten tips. At the CINaM, 0.38 mm thick tungsten wires were etched in a NaOH solution (8.5 g NaOH in 50 ml water, 6.5 mA cutting current at +4.0 V).

nc-AFM (CINaM) - Noncontact AFM was accomplished in the frequency modulation mode (self-excitation)[8]. Two conducting silicon cantilevers (NanoWorld AG, Neuchatel, Switzerland) with resonance frequencies of 75.2 and 78.1 kHz (PPP-QFMR, n^+-Si, 0.01-0.02 Ω cm) were used, as well as two cantilevers with resonance frequencies of 300 and 314.8 kHz (PPP-QNCHR, n^+-Si, 0.01-0.02 Ω cm). The peak-to-peak amplitude was kept constant during imaging. To precisely measure the frequency shift $\triangle f$, a digital demodulator (EasyPLL, NanoSurf, Liestal, Switzerland) replaced the analogeous demodulator from the SCALA electronics.

KPFM (CINaM) - Kelvin probe force microscopy (KPFM) was done in the frequency modulation mode[9]. A dc bias voltage (U_{bias}) and ac voltage (U_{ac} between 150 and 250 mV) with a frequency of $f_{\mathrm{ac}} = 476$ Hz were applied at the sample (tip grounded). In a KPFM experiment, the electrostatic tip-surface interaction is minimized at each point on the surface by the bias voltage, which yields the contact potential difference (CPD) between tip and surface defined as $\mathrm{CPD} = U_{\mathrm{bias},0} = (\phi_{\mathrm{sample}} - \phi_{\mathrm{tip}})/e$ for the set-up used in Marseille. If at two different locations on the surface (Position 1 and 2) the CPD is measured, the CPD difference $\triangle\mathrm{CPD} = \mathrm{CPD}_1 - \mathrm{CPD}_2 = ((\phi_1 - \phi_{\mathrm{tip}}) - (\phi_2 - \phi_{\mathrm{tip}}))/e = (\phi_1 - \phi_2)/e = \triangle\phi/e$ yields the work function (WF) difference $\triangle\phi_{1-2} = \phi_1 - \phi_2$ between the two surface locations[10]. KPFM is applied during the constant frequency nc-AFM imaging mode so that a topography and *WF image* of the CPD are simultaneously obtained. A bright contrast in WF images corresponds to a high WF whereas a dark contrast corresponds to a low WF. By definition (see above), a WF image represents variations and differences of the local surface WF.

XPS (NANO) - The XPS measurements were conducted with a conventional double anode Mg/Al X-

ray source (RQ 20/38, Leybold/Specs, Germany), using Al K_α photons, and a hemispherical electron analyzer (EA 125, ScientaOmicron, Taunusstein, Germany). Photoelectrons were detected at an emission angle of 65° from the sample normal to increase the surface sensitivity. The analysis of the Ce3d photoemission spectra was conducted following the procedure introduced by Skála and co-workers [11,12].

LEED (NANO + CINaM) - In both laboratories, the same type of LEED apparatus (SPECTALEED, ScientaOmicron, Taunusstein, Germany) was used. Each LEED optic has 4 grids whereas a W/Th (CINaM) and LaB_6 filament (NANO) are used. In the energy range between 40 and 100 eV, an image of the LEED pattern was taken each 5 eV. All images were subtracted by an image that contained only the background (LEED image without sample). Note that the WTh filament is probably not well aligned and/or bent, which explains that the LEED background is higher than the one of the LEED with the LaB_6 filament. Furthermore, due to different sample-to-LEED distances of the two apparatus (W/Th and LaB_6), the images might be differently distorted, which could explain the slight deviations in the Pt/ceria ratio mentioned in the main manuscript.

3 CHOICE OF WF AND LATTICE CONSTANT VALUES

We use the following lattice constants for palladium (a_{Pt}) and cerium oxide in its fully oxidized form (CeO_2):

$$\begin{aligned} a_{\mathrm{Pt,lit}} &= 3.92 \pm 0.01 \text{ Å} \\ a_{\mathrm{CeO2,lit}} &= 5.41 \pm 0.01 \text{ Å} \end{aligned}$$

The values are an average of several experimental values taken from literature. The values were obtained by X-ray scattering (see Table S2 for Pt and Table S3 for CeO_2). For Pt, we also list theoretical values from literature, which were obtained by density functional theory (DFT), either computed with the local density approximation (LDA), generalized gradient approximation (GGA) or with other methods. The mean value of the theoretical values ($a_{\mathrm{Pt,lit,theo}} = 3.96$ Å) compares well with the mean value from experiments ($a_{\mathrm{Pt,lit,exp}} =$ 3.917 Å). With respect to CeO_2, DFT values for the lattice constant $a_{\mathrm{CeO2,lit,theo}}$ vary significantly, from 5.36 to 5.69 Å as summarized in Ref. 13. For the absolute WF of Pt(111), we use the following mean value:

$$\phi_{\mathrm{Pt(111),\ lit}} = 5.9 \pm 0.1 \text{ eV}$$

The value is averaged over several experimental values from literature (see Table S4), which are also partially listed in Ref. 49. Because the values scatter within a WF range between 5.7 and 6.0 eV we assume

Table S2: Experimental and DFT literature values for the lattice constant $a_{\mathbf{Pt}}$ of platinum (Å), with the experimental ($a_{\mathbf{Pt,lit,exp}}$) and theoretical mean values ($a_{\mathbf{Pt,lit,theo}}$).

Material	a	Experiment	Reference
Pt	3.930	X-ray	14
Pt	3.878	X-ray	15
Pt	3.912 ± 0.004	X-ray	16
Pt	3.911	X-ray	17
Pt	3.944	X-ray	18
Pt	3.9158	X-ray	19
Pt	3.924	X-ray	20
Pt	3.922	X-ray	21
Mean value	$3.917 = a_{\mathrm{Pt,lit,exp}}$		
Pt	3.99	GGA (PW91)	22
Pt	3.99	GGA (PW91)	23
Pt	3.89	LDA	24
Pt	3.97	GGA (PBE)	
Pt	3.92	See §	25
Pt	3.986	GGA (PBE)	26
Pt	3.985	GGA (PW91)	27
Pt	3.91	See ¶	28
Mean value	$3.96 = a_{\mathrm{Pt,lit,theo}}$		

a 'safe error' of 0.1 eV, as it is done in Ref. 49. We consider experimental WF values, which were obtained exclusively in UHV, either by field emission (FET) or photo-electron-threshold-yield techniques (PETY), by ultraviolet photoelectron spectroscopy (UPS) or angle-resolved UPS (ARUPS).

Table S3: Experimental literature values for the lattice constant $a_{\mathbf{CeO2}}$ of $\mathbf{CeO_2}$ (Å). The experimental mean value is given by $a_{\mathbf{CeO2,lit,exp}}$.

Material	a	Experiment	Reference
CeO_2	5.411	X-ray	29
CeO_2	5.406	X-ray	30
CeO_2	5.411	X-ray	31
CeO_2	5.411 ± 0.001	X-ray	32
CeO_2	5.41	X-ray	33
Mean value	$5.411 = a_{\mathrm{CeO2,lit,exp}}$		

§Several different functionals (LDA, PBE, PBEsol, etc.). We only considered the four values in bold of table I.

¶Several different functionals. As recommended, we only consider an averaged value from PBEsol, SCAN, SCAN + rVV10.

Table S4: Experimental and DFT literature values for the work function ϕ (eV) of the Pt(111) surface. A mean value is listed for the experimental values ($\phi_{\mathbf{Pt(111),lit,exp}}$) as well as for the theoretical values ($\phi_{\mathbf{Pt(111),lit,theo}}$).

Surface	ϕ	Exp.eriment	Reference
Pt(111)	5.95 ± 0.05	FET	34
Pt(111)	5.99	FET	35
Pt(111)	5.7 ± 0.2	UPS	36
Pt(111)	5.6 ± 0.1	UPS	37
Pt(111)	5.7 ± 0.2	UPS	38
Pt(111)	6.08 ± 0.15	UPS	39
Pt(111)	5.9	UPS	40
Pt(111)	5.95 ± 0.1	UPS	41
Pt(111)	5.84 ± 0.05	UPS	42
Pt(111)	6.10 ± 0.06	PETY	43
Pt(111)	5.8	ARUPS	44
Pt(111)	5.85 ± 0.05	UPS	45
Mean value	$5.86 = \phi_{\mathrm{Pt(111),lit,exp}}$		
Pt(111)	5.63	GGA (PW91)	23
Pt(111)	6.05	LDA	24
Pt(111)	5.71	GGA (PBE)	
Pt(111)	5.69	GGA (PBE)	46
Pt(111)	6.13	LDA	47
Pt(111)	5.76	GGA (PBE)	26
Pt(111)	5.70	GGA (PBE)	48
Pt(111)	5.97	SCAN, see ‖	28
Mean value	$5.83 = \phi_{\mathrm{Pt(111),lit,theo}}$		

We compare the experimental values also with values from DFT, which were computed either in the local density approximation (LDA) or generalized gradient approximation (GGA) or with other methods. The mean theoretical value ($\phi_{\mathrm{Pt(111),lit,theo}} = 5.83$ eV) compares very well with the experimental one ($\phi_{\mathrm{Pt(111),lit,exp}} = 5.86$ eV).

‖Several different functionals. As recommended, we only consider an averaged value from PBEsol, SCAN, SCAN + rVV10.

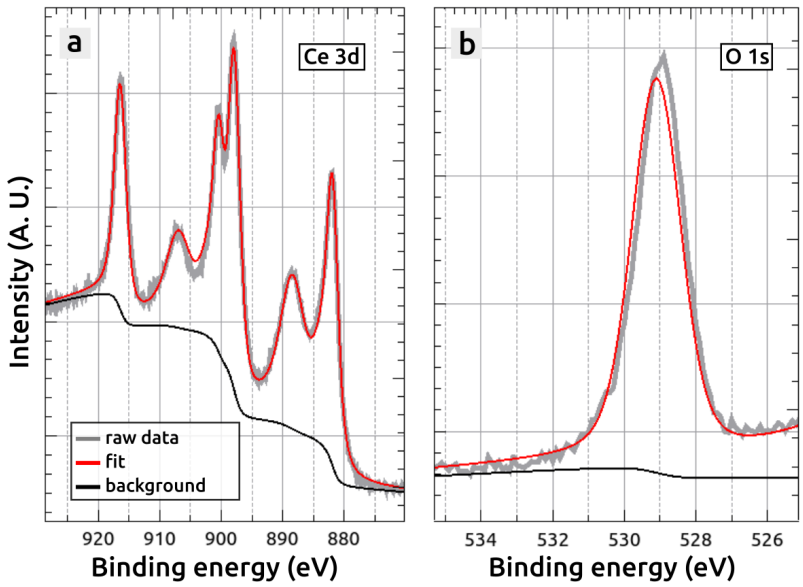

Figure S1: X-ray photoemission Ce3d (a) and O1s (b) spectra, right after the preparation of the ceria film (evaporation of Ce onto Pt(111) kept at RT, evaporation rate: $\sim$0.2 Å/min, post-annealing at 770 °C in 1×10^{-7} mbar O_2 for 15 min, nominal thickness: 2.3 ML). The gray and red spectra show the raw data and the fits. The black line shows the background contribution.

4 SUPPORTING EXPERIMENTS

4.1 XPS of the as-prepared ceria film

Figure S1 shows the Ce3d (a) and O1s (b) spectra of the ceria film right after its preparation in the UHV chamber in Modena. An analysis of the Ce3d spectrum yields a negligible Ce^{3+} concentration (c_{Ce3+} = 1 %). While the precision of the Ce^{3+} concentration is quite high, within $\pm$1-2 %, its accuracy is certainly above $\pm$5%. The O1s spectrum shows a perfect symmetric shape of oxygen, which is bound to Ce^{4+} [50,51]. No signature for oxygen bound to Ce^{3+} is found. The carbon C1s peak was below the detection limit.

4.2 XPS analysis of O1s spectra

In Table S5, we show the results of the XPS analysis, which was done with the O1s spectra shown in Figure 2b of the main article. The peak areas are listed for the as-introduced ceria film, same film after an oxidation and following reduction in Modena. In the main article, we assign peak 1 to oxygen at Ce^{4+} [50,51], peak 2 to oxygen at Ce^{3+} [50,51] and peak 3 to hydroxyls and/or H_2O molecules [52,53].

As it can be seen, the as-introduced film contained a large amount of hydroxyls and/or H_2O molecules, which could be entirely removed by the oxygen annealing. After the reduction, peak 3 remained below the

Table S5: Peak areas of the O1s spectra shown in Figure 2b of the main article. The units are arbitrarily chosen. More details can be found in the text.

	Area peak 1 at 529.1 eV	Area peak 2 at 530.1 eV	Area peak 3 at 531.5 eV
As introduced	23861	5722	8901
After oxidation	24111	7728	0
After reduction	18308	11605	0

detection limit. However, due to the reduction of the ceria film, the amount of oxygen bound to Ce^{3+} (peak 2) and Ce^{4+} (peak 1) increased and decreased, respectively.

4.3 Reduction at 700 °C

Figure S2 shows the ceria film after the second reduction by UHV annealing in the first redox cycle. Both images are the same and show the topography, whereas the green mask in image Figure S2b represents the coverage of the ceria film ($\sigma_{\mathrm{rCeria}} \approx 56$ %). The image was obtained in the noncontact mode of the AFM.

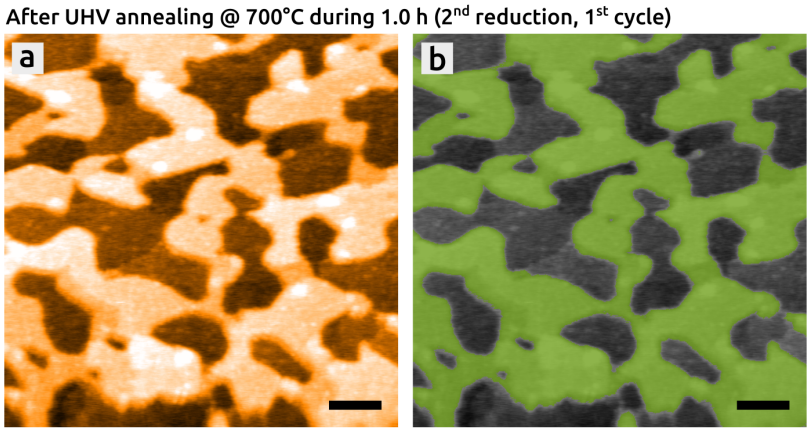

Figure S2: Morphology of the 2.3 ML ultra-thin ceria film after the second reduction in the first redox cycle (nc-AFM topography images). More details can be found in the text. Scanning parameters: $\triangle f = -9.3$ Hz, $f_0 = 75.2$ kHz, $v = 0.5$ Hz, scale bars: 20 nm.

4.4 Analysis of height differences

For the determination of height differences, noncontact AFM yields accurate values, in particular if the Kelvin technique is applied during the imaging - KPFM corrects artificial height changes that may arise due to, e.g., variations of the surface WF[54] or due to residual surface charges[55]. The images shown in Figure 5a and c of the main article were obtained with the Kelvin mode switched on so that they can be used for measuring height differences. The same images are represented in Figure S3.

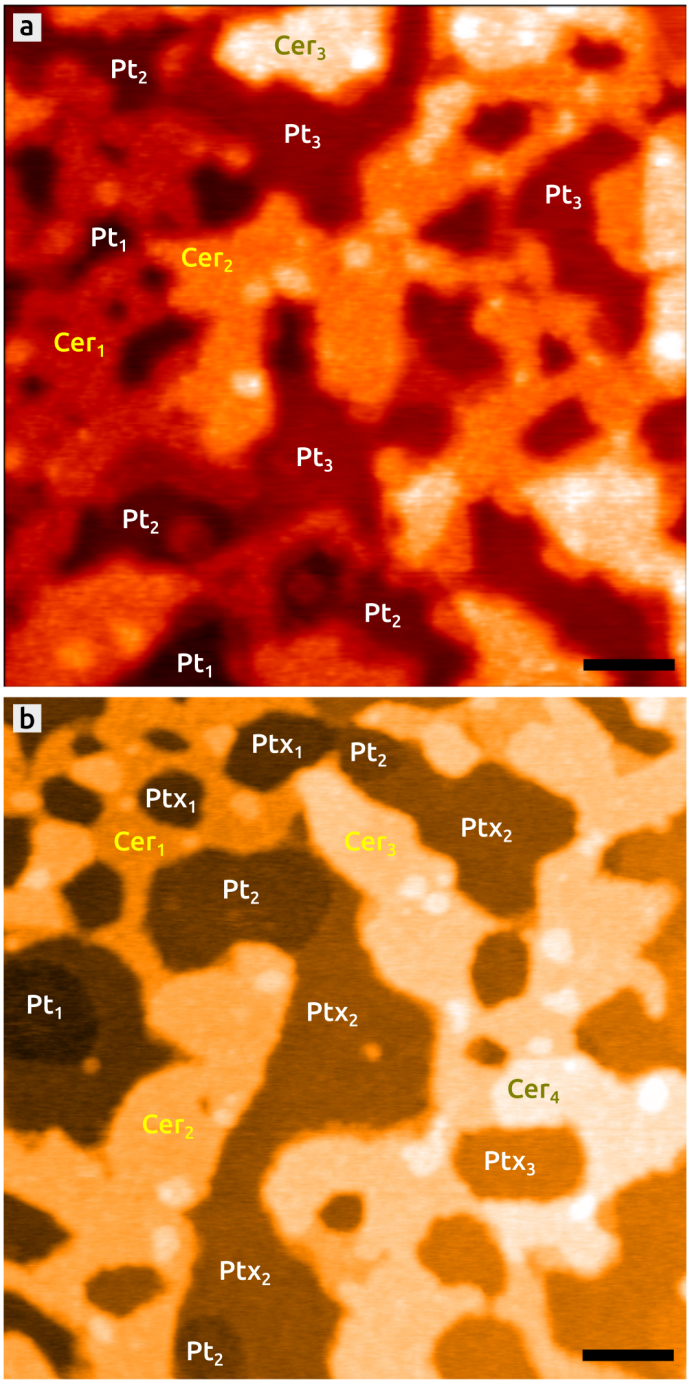

Figure S3: Topography nc-AFM images of the oxidized (a) and reduced film (b), acquired in the second redox cycle discussed in the main article. The images are the same as used for Figure 5a and c. In both images, different regions of the uncovered Pt(111) and alloyed support as well as different ceria islands are labeled with Pt_n, Ptx_n and Cer_n. The absolute z positions of each region are listed in Table S6. Scale bars: 10 nm.

Table S6: The absolute z piezo displacement (in nm) for each region, which is visible in the topography image obtained on the oxidized (Figure S3a) and reduced ceria film (Figure S3b). For each film, the height difference (h) between regions of the support are listed (in Å). For the reduced ceria film, values in or without brackets correspond to the case Ptx ≡ Pt(111) and Pt ≡ Pt(111), respectively.

Oxidized film			
Region	z	Region	z
Pt_1	−1.06	Cer_1	−0.39
Pt_2	−0.83	Cer_2	−0.03
Pt_3	−0.61	Cer_3	0.33
$\lvert h_{Pt1\text{-}Pt2}\rvert$	2.37	$\lvert h_{Pt1\text{-}Pt3}\rvert$	4.54
$\lvert h_{Pt2\text{-}Pt3}\rvert$	2.16	$\lvert h_{\mathbf{Pt,mean}}\rvert$	2.27
Reduced film			
Region	z	Region	z
Pt_1	−1.99 (−1.78)	Cer_1	−1.22 (−1.09)
Pt_2	−1.76 (−1.58)	Cer_2	−0.88 (−0.79)
Ptx_1	−1.83 (−1.64)	Cer_3	−0.63 (−0.56)
Ptx_2	−1.60 (−1.43)	Cer_4	−0.34 (−0.31)
Ptx_3	−1.33 (−1.19)	$\lvert h_{Ptx1\text{-}Ptx2}\rvert$	2.38 (2.13)
$\lvert h_{\mathbf{Pt1\text{-}Pt2}}\rvert$	2.27 **(2.03)**	$\lvert h_{Ptx2\text{-}Ptx3}\rvert$	2.69 (2.41)
$\lvert h_{Pt1\text{-}Ptx1}\rvert$	1.55 (1.39)	$\lvert h_{Ptx1\text{-}Ptx3}\rvert$	5.06 (4.54)
$\lvert h_{Pt2\text{-}Ptx1}\rvert$	0.72 (0.64)	$\lvert h_{\mathbf{Ptx,mean}}\rvert$	2.53 **(2.27)**
$\lvert h_{Pt2\text{-}Ptx2}\rvert$	1.66 (1.49)		

Each image was corrected such that regions of the support and film are perpendicular to the view (horizontal profiles of terraces). With help of the Gwyddion software [5], a mask is then drawn on a terrace of choice and the mean value of the absolute z piezo deflection is taken from only the masked region. The values of all regions (Pt_n, Ptx_n and Cer_n) visible in both images in Figure S3 are listed in Table S6.

The z values of each of the two images were calibrated such that the height differences of only the uncovered support yield a multiple of the single Pt(111) step height, with $h_{Pt} = a_{Pt,lit}/\sqrt{3} \approx 2.26$ Å (for $a_{Pt,lit}$ see Table S2). The calibration of the image obtained on the oxidized film (Figure S3a) is relatively easy in comparison to the image obtained on the reduced film (Figure S3b) where two types of supports (Pt and Ptx) can be found.

Table S7: Height differences h (in Å) between the Pt support and the ceria islands, obtained from the three ceria islands and the three Pt(111) terraces in the topography image of the *oxidized ceria film* (Figure S3a). The stacking sequence and the related Pt(111) terrace that supports a ceria film (left) are mentioned on the right. At the end of the table, the height differences between the three ceria islands are listed.

		Oxidized film		
Ceria	Pt	h	Stacking	Support
Cer_1	Pt_1	6.79	$2\times h_{Cer}$	Pt_1
	Pt_2	4.41	$2\times h_{Cer} - 1\times h_{Pt}$	
	Pt_3	2.25	$2\times h_{Cer} - 2\times h_{Pt}$	
Cer_2	Pt_1	10.40	$2\times h_{Cer} + 2\times h_{Pt}$	Pt_3
	Pt_2	8.03	$2\times h_{Cer} + 1\times h_{Pt}$	
	Pt_3	5.86	$2\times h_{Cer}$	
Cer_3	Pt_1	13.97	$3\times h_{Cer} + 2\times h_{Pt}$	Pt_3
	Pt_2	11.60	$3\times h_{Cer} + 1\times h_{Pt}$	
	Pt_3	9.44	$3\times h_{Cer}$	
$\lvert h_{Cer1\text{-}Cer2}\rvert$		3.61	$2h_{Pt}$	
$\lvert h_{Cer2\text{-}Cer3}\rvert$		3.58	$3h_{Cer} - 2h_{Cer} = h_{Cer}$	
$\lvert h_{Cer1\text{-}Cer3}\rvert$		7.19	$3h_{Cer} - 2h_{Cer} + 2h_{Pt} = h_{Cer} + 2h_{Pt}$	

Oxidized film

Although the quality of the image recorded on the *oxidized film* (Figure S3a) is rather low, a height analysis can still be done, with an experimental error of around $\triangle z_{err} = \pm 0.5$ Å. The mean value of the height differences taken from only the uncovered support was adjusted such it equals the single step height of Pt(111): $h_{Pt} = h_{Ptn,mean}$ (red bold value in Table S6). As it can be seen, the individual height values between the three Pt(111) terraces ($|h_{Pt1\text{-}Pt2}|$, $|h_{Pt1\text{-}Pt3}|$ and $|h_{Pt2\text{-}Pt3}|$ in red) match well expected integer values of the height h_{Pt} within the experimental error.

Table S7 lists all relevant height differences h between the three ceria islands, Cer_1, Cer_2 and Cer_3, and all three Pt(111) terraces, Pt_1, Pt_2 and Pt_3 (see Figure S3a). Furthermore, a possible stacking and the related Pt(111) terrace that supports a respective ceria island (on the left) are shown on the right side. As it can be seen, only a more or less rough estimation can be given of how a ceria island is supported on a Pt(111) surface. Within the experimental error, it can be assumed that the Cer_1 island is supported on the neighbouring Pt_1 terrace, while Cer_2 and Cer_3 are supported on the Pt_3 terrace, with Cer_1 and Cer_2 having a double ML height and Cer_3 having a triple ML height. Because the ceria islands are supported on two different Pt(111) terraces and they also have a different height (see Figure S4b), the height differences

between the ceria islands is not necessarily an integer value of the ceria ML height (see values in red in Table S7).

Reduced film

The quality of the image in Figure S3b, which was acquired on the *reduced film*, is considerably better than the one in Figure S3a, and we can assume an error of around $\triangle z_{\mathrm{err}} = \pm 0.3$ Å. However, despite the smaller error the analysis of height differences and the related interpretation remain challenging due to the two existing support regions, Pt and Ptx.

In the analysis, either the Pt or Ptx regions are assumed to be the clean Pt(111) support. In the case of **Pt ≡ Pt(111)**, only two Pt(111) terraces exist with $|h_{\mathrm{Pt1\text{-}Pt2}}|$ calibrated to $h_{\mathrm{Pt}} \approx 2.26$ Å (Table S6). In comparison, the height of a single Ptx step (values in blue) is larger by 0.27 Å (see Figure S4a) and measures in mean $h_{\mathrm{Ptx,mean}} \approx 2.53$ Å (value in bold blue). In contrast, if the Ptx regions are assumed to be Pt(111) terraces (**Ptx ≡ Pt(111)**), the Pt regions would have a step height of about ~ 2.0 Å, which corresponds to a contraction of $2.0/2.26 \approx 10$ % with respect to h_{Pt}.

With respect to the height differences between the Pt and Ptx regions (orange values in Table S6) it can be concluded that the relative height of the Ptx regions is not exactly in the middle of the height formed by two Pt regions (see Figure S4a): values between $h_{\mathrm{Pt\text{-}Ptx}} \approx 0.7$ and ~ 1.6 Å can be found ($h_{\mathrm{Pt\text{-}Ptx}} \approx 0.6$ and ~ 1.45 Å for Ptx ≡ Pt(111)). Note that because the height values of the single steps are different ($h_{\mathrm{Pt}} \approx 2.26$ Å and $h_{\mathrm{Ptx}} \approx 2.53$ Å) it seems that *a priori* the height difference between the Pt and Ptx regions cannot be a geometrically well-defined value. The reason for this is unknown.

The experimental values of the height differences between the support and the ceria islands are listed in Table S8, distinguishing again both cases, Pt ≡ Pt(111) (values in black) and Ptx ≡ Pt(111) (red values in brackets). Figure S4b shows all possible height differences, which may appear between the Pt(111) support and ceria islands with different heights. Note that we only consider up to 4 ML high ceria islands, which is still somewhat compatible with the nominal amount of deposited ceria (2.3 ML) onto Pt(111), covering a fraction of 70 % of the surface. Furthermore, we only consider Pt(111) steps with a maximum height of $\leq 2\,h_{\mathrm{Pt}}$, which are either underneath or aside a ceria island - higher Pt steps are only rarely observed on the clean Pt(111) surface. In principle, height values of 0.86, 1.72, 3.12, 5.38, 6.24, 7.64, 8.50, 9.36, 10.76, 11.62, 12.48, 13.88, 14.74 and 17.00 Å can be found for different stacking combinations of ceria islands and Pt layers either underneath or aside.

A comparison of the experimental with the expected values shows that it is almost impossible to state, which one of the two calibrations (Pt ≡ Pt(111) or Ptx ≡ Pt(111)) yields a more credible result. Tentatively,

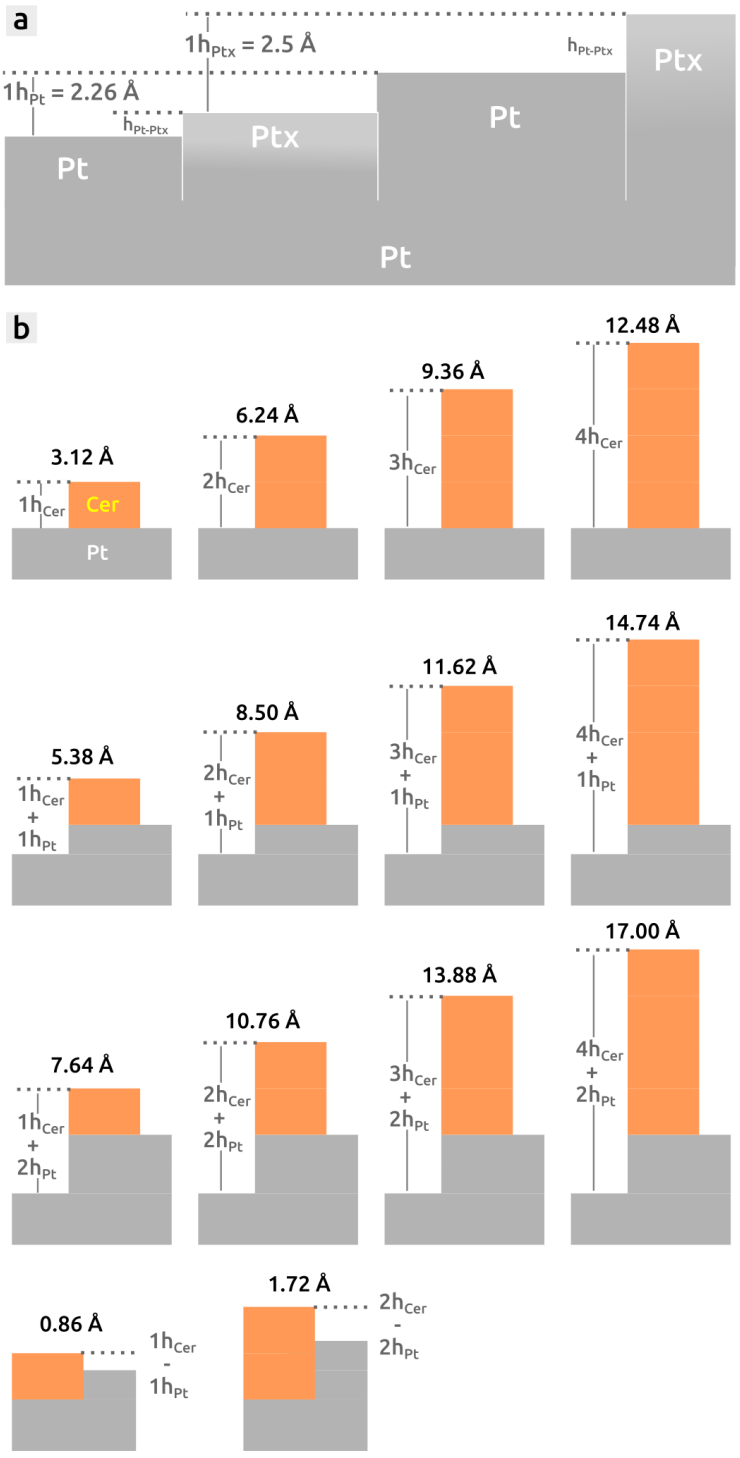

Figure S4: (a) Height differences between the two different support regions, Pt and Ptx, observed on the sample of the *reduced ceria film*. (b) Expected height differences between Pt(111) and ceria islands in several different stacking configurations. It is assumed that an ceria island has an integer value of the triple layer height of CeO_2 ($a_{CeO2}/\sqrt{3} = 3.12$ Å, with a_{CeO2} from Table S3). For a single Pt(111) step, a height of 2.26 Å is used (for a_{Pt} see Table S2).

Table S8: Height differences h (in Å) between the support and the ceria islands, obtained from the four ceria islands and the five Pt(x) terraces in the topography image of the *reduced ceria film* (Figure S3b). Black and red values in brackets correspond to the case Pt ≡ Pt(111) and Ptx ≡ Pt(111), respectively. A possible stacking sequence is mentioned on the right. At the end of the table, the height differences between the three ceria islands are listed.

	Reduced film		
Ceria	Pt	h	Possible stacking
Cer_1	Pt_1	7.68 (6.88)	$1\times h_{Cer} + 2\times h_{Pt}$
	Pt_2	5.41 (4.85)	$1\times h_{Cer} + 1\times h_{Pt}$
	Ptx_1	6.13 (5.49)	$2\times h_{Cer}$ $1\times h_{Cer} + 1\, h_{Pt}$
	Ptx_2	3.75 (3.36)	$1\times h_{Cer}$
	Ptx_3	1.07 (0.95)	$1\times h_{Cer} - 1\times h_{Pt}$ $1\times h_{Cer} - 1\ \times\ h_{Pt}$
Cer_2	Pt_1	11.09 (9.94)	$2\times h_{Cer} + 2\times h_{Pt}$
	Pt_2	8.82 (7.91)	$2\times h_{Cer} + 1\times h_{Pt}$ $1\times h_{Cer} + 2\, h_{Pt}$
	Ptx_1	9.54 (8.55)	$3\times h_{Cer}$ $2\times h_{Cer} + 1\, h_{Pt}$
	Ptx_2	7.16 (6.42)	$2\times h_{Cer}$
	Ptx_3	4.48 (4.01)	/
Cer_3	Pt_1	13.62 (12.21)	$3\times h_{Cer} + 2\times h_{Pt}$ $4\times h_{Cer}$
	Pt_2	11.35 (10.18)	$3\times h_{Cer} + 1\times h_{Pt}$
	Ptx_1	12.07 (10.82)	$2\times h_{Cer} + 2\, h_{Pt}$
	Ptx_2	9.69 (8.69)	$3\times h_{Cer}$ $2\times h_{Cer} + 1\, h_{Pt}$
	Ptx_3	7.01 (6.28)	$2\times h_{Cer}$
Cer_4	Pt_1	16.46 (14.76)	too high
	Pt_2	14.20 (12.72)	too high
	Ptx_1	14.91 (13.37)	$4\times h_{Cer} + 1\times h_{Pt}$
	Ptx_2	12.54 (11.24)	$4\times h_{Cer}$
	Ptx_3	9.85 (8.83)	/
$\lvert h_{Cer1\text{-}Cer2}\rvert$		3.41 (3.06)	
$\lvert h_{Cer1\text{-}Cer3}\rvert$		5.94 (5.33)	
$\lvert h_{Cer1\text{-}Cer4}\rvert$		8.78 (7.87)	
$\lvert h_{Cer2\text{-}Cer3}\rvert$		2.53 (2.27)	
$\lvert h_{Cer2\text{-}Cer4}\rvert$		5.37 (4.82)	
$\lvert h_{Cer3\text{-}Cer4}\rvert$		2.84 (2.55)	

a slightly more convincing result yields the case Pt ≡ Pt(111) (black values): we find 1, 2 and 3 ML high ceria islands measured from the Pt regions, whereas smaller island heights of 1 and 2 ML are found for the Ptx regions.

4.5 Coverage of oxidized and reduced ceria on Pt(111)

In the main article, we describe changes of the surface coverage of the ceria film upon a redox step. Here we explain how we have determined the surface coverage in general, by using one example.

Figure S5 shows the ceria film after the annealing in oxygen (a,b) and reduction in UHV (c,d). The measurements were both done in the *second redox cycle* (see Figure 3e and f and Figure 5 of the main article). The four images in the left row (a,c) show the surface topography whereas the four images in the right row (b,d) represent the surface WF (KPFM). The two images at the bottom of Figure S5a,c are duplicates of the images above. The same applies for Figure S5b,d. In contrast to the images shown in the main article, the KPFM images here show a larger surface area of 300×300 nm^2, which increases the statistics of the analysis. All values of the surface coverage presented in the main article were obtained with images of this size.

With help of the 'Mark by Threshold' routine in the Gwyddion software[5] (Menu → Data Process → Grains → Mark by Threshold), the film can be easily marked in each topography (a,c) and WF image (b,d), where regions with a low WF correspond to the ceria film, as stated in the main article. The Gwyddion software then computes the coverage in percentage of the masked regions. For the oxygen annealed ceria film (a,b) the following average coverage is found:

$$\sigma_{\mathrm{CeO2}} = (70 \pm 6)\ \%$$

As it can also be easily seen by a comparison of the images (a with c, and b with d), the coverage of the reduced ceria film (c,d) is smaller :

$$\sigma_{\mathrm{rCeria}} = (54 \pm 4)\ \%$$

The very bright regions (very high WF) in the WF image in Figure S5d cover only a very small part of the entire surface:

$$\sigma_{\mathrm{rCeria\_Pt}} = (5 \pm 4)\ \%$$

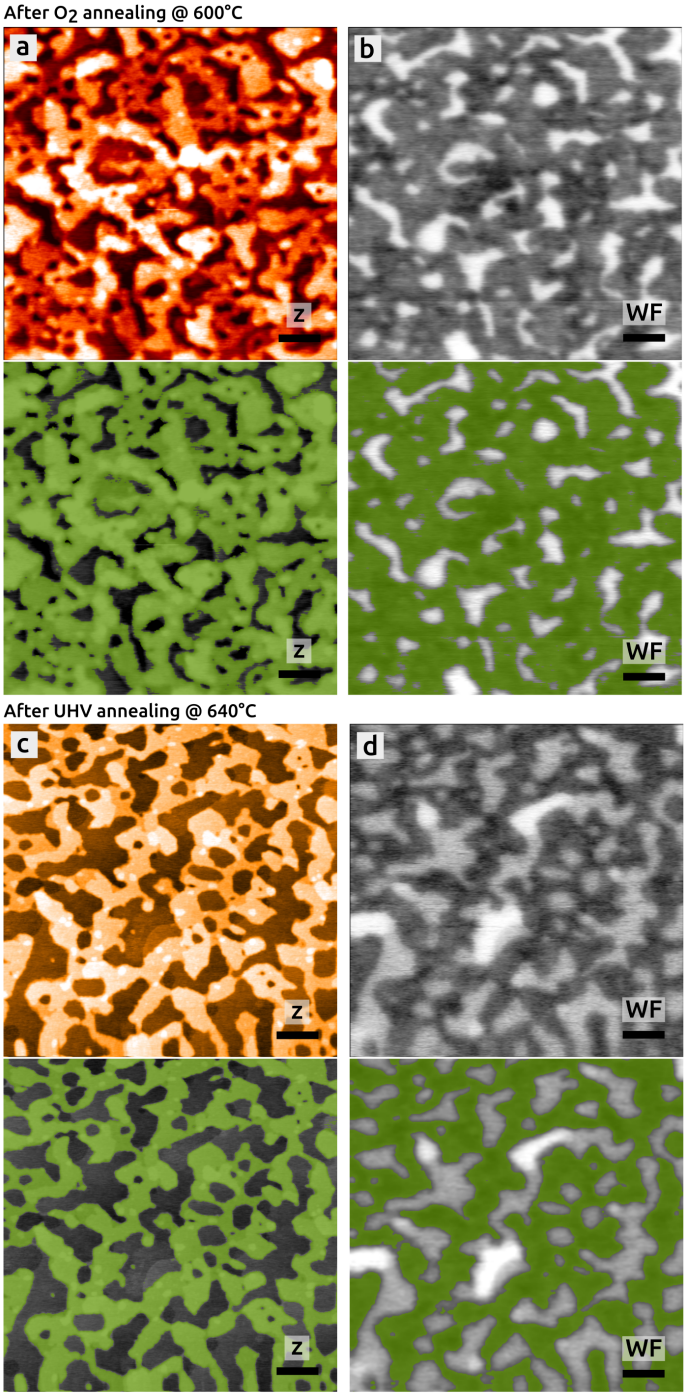

Figure S5: Analysis of two KPFM measurements of the 2.3 ML ultra-thin ceria film after its oxidation (a,b) and following reduction (c,d), during the second redox cycle. One KPFM measurement is represented by four images in a column (e.g., a and b). The four images on the top are topography images (a,c), whereas the other four images at the bottom (b,d) are WF images. The images with the green mask are duplicates of the respective images above. The KPFM measurement in (a) and (b) was obtained during the same SPM session as the measurement shown in Figure 5a and b of the main article. The same applies for the KPFM measurement in (c) and (d), which corresponds to Figure 5c and d of the main article. (a) $\triangle f = -14.5$ Hz, (b) $\triangle f = -18.8$ Hz, all: $f_{\mathrm{ac}} = 650$ Hz, $U_{\mathrm{ac}} = 500$ mV, $v = 0.5$ Hz, scale bars: 50 nm.

Table S9: Experimental values of the coverage obtained from the images shown in Figure S5.

	Topography	WF
(a,b)	$\sigma_{\mathrm{CeO2}} = 68 \pm 6\%$	$\sigma_{\mathrm{CeO2}} = 71 \pm 6\%$
(c,d)	$\sigma_{\mathrm{rCeria}} = 54 \pm 4\%$	$\sigma_{\mathrm{rCeria}} = 56 \pm 7\%$

Note that there is a good agreement between the topography and WF image (see Table S9). However, for all measurements we only take the values from the topography images because the film surface area is mostly better defined in a topography than in a WF image. In a WF image, the ceria islands look mostly smeared out, which is due to the larger tip-surface convolution effect in KPFM in comparison to nc-AFM, as explained in great detail in Ref. 56.

With respect to the error, the coverage can change form surface site to surface site. Furthermore, in some cases the error can be large due to a limited image quality. Overall, we assume a 'safe' error of ~ 6 % whereas this error can also sometimes be larger. Nevertheless, the objective of our work is to show trends in the change of the surface coverage. The precision here is completely sufficient for the latter purpose.

4.6 Analysis of the surface coverage

The ceria film area and therefore the effective amount of ceria decreases during a reduction step. Because oxygen leaves the surface, it is only the released cerium atoms that remain on the surface. In the main article, we propose that these cerium atoms are built into the Pt(111) support to form a $CePt_5$-like alloy. The main questions are: (i) how many cerium atoms get released and are distributed onto the support for the alloy formation? (ii) how large is the surface coverage of the alloy?

We consider two models: in the first model, the effective coverage of a one monolayer thin $CePt_5$ alloy ($\sigma_{\mathrm{rCeria\_alloy}}$) is calculated from the experimental ceria coverage of the oxidized (σ_{CeO2}) and reduced film (σ_{rCeria}). In the second model, the coverage $\sigma_{\mathrm{rCeria\_alloy}}$ is calculated from the ceria coverage σ_{CeO2} alone, under the assumption of a balance between the coverages of the reduced ceria film and the uncovered alloy. At the end of this subsection, the results of both models are discussed.

4.6.1 Model 1

Consider a given surface area of, e.g., the entire sample surface ($A \approx 1$ cm^2) and that the ceria film is oxidized, covering the entire Pt(111) sample by σ_{CeO2} percent. The respective surface area of ceria is then:

$$A_{\mathrm{CeO2}} = A\,\sigma_{\mathrm{CeO2}}$$

Now we consider the number of cerium atoms of the CeO_2 monolayer (ML) at the interface with the Pt(111) support: it has to be the ceria surface area A_{CeO2} times the density of cerium atoms in the ML (ϱ_{CeO2}, e.g., in units [atoms/cm^2]). Because the islands have a mean height of 2 ML, we have to multiply by 2 to obatin the total amount of cerium atoms (N_{CeO2}) in the ceria islands:

$$N_{CeO2} = 2\, A_{CeO2}\, \varrho_{CeO2} = 2\, A\, \sigma_{CeO2}\, \varrho_{CeO2} \tag{1}$$

In the same surface area A, we make the same consideration for the reduced film, with the density ϱ_{rCeria} of cerium atoms in reduced ceria:

$$\begin{aligned} A_{rCeria} &= A\, \sigma_{rCeria} \\ N_{rCeria} &= 2\, A\, \sigma_{rCeria}\, \varrho_{rCeria} \end{aligned} \tag{2}$$

The number of cerium atoms $N_{Ce,free}$, which get released due to the shrinking of the ceria islands during the reduction, is:

$$N_{Ce,free} = N_{CeO2} - N_{rCeria} \tag{3}$$

We now consider an alloyed $CePt_5$/Pt(111) surface: let's assume that only one subsurface $CePt_2$ layer of $CePt_5$ is formed and that the lowest energy configuration is given by Pt_4/$CePt_2$/Pt_3/Pt(111) (from Ref. 48, see Figure S6b). The number of cerium atoms contained in a monolayer of the alloy, which fully covers the surface, is:

$$N_{Alloy} = A\, \varrho_{Alloy} \tag{4}$$

With this, we can calculate the effective surface coverage of the alloyed surface, which would be formed by the released cerium atoms after the reduction of the ceria film. With Eq. (3) and (4) we obtain:

$$\sigma_{rCeria\_alloy} = \frac{N_{Ce,free}}{N_{Alloy}} = 2\, \frac{\sigma_{CeO2}\, \varrho_{CeO2} - \sigma_{rCeria}\, \varrho_{rCeria}}{\varrho_{Alloy}} \tag{5}$$

With the help of the known densities of cerium in CeO_2, reduced ceria and $CePt_5$ (see below), the surface coverage of the *alloy* (σ_{rCeria_alloy}) can be calculated from the experimental values of the ceria coverage of the oxidized (σ_{CeO2}) and reduced ceria film (σ_{rCeria}).

With respect to the cerium densities, ϱ_{CeO2} is easy to calculate (Figure S6a) whereas ϱ_{rCeria} can be

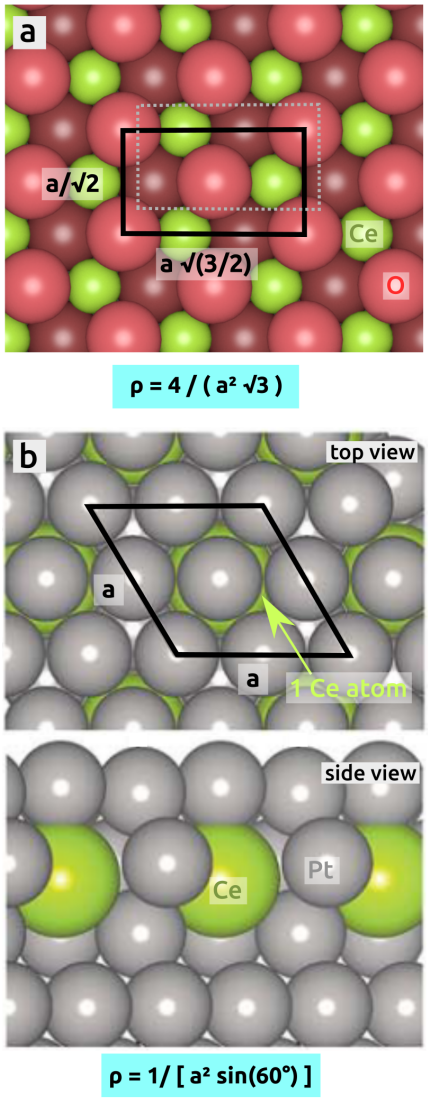

Figure S6: Lattice models for $CeO_2(111)$ in a top view (a) and $CePt_5$ on Pt(111) in a top and side view (b) for the determination of the densities ϱ_{CeO2} (a) and ϱ_{Alloy} (b). The alloy is in its lowest energy configuration (from Ref. 48). The black rectangle (a) and rhombus (b) show the surface area $A_{CeO2} = (a^2_{CeO2}\sqrt{3})/2$ and $A_{CePt5} = a^2_{CePt5}\sin(60°)$, respectively, which are used to calculate the densities ϱ: for $CeO_2(111)$, two Ce atoms can be found in the rectangle (see dotted gray rectangle) so that $\varrho_{CeO2} = 2/A_{CeO2}$. For $CePt_5$ one Ce atom can be found in the rhombus (b) which yields $\varrho_{CePt5} = 1/A_{CePt5}$.

obtained by just considering a correction factor λ. The latter, however, seems to be almost 1 ($\varrho_{\mathrm{rCeria}} \approx \varrho_{\mathrm{CeO2}}$) for reduced ceria films because if we assume a $(4\times4)_{\mathrm{Pt}}/(3\times3)_{\mathrm{Ceria}}$ structure (see main article) and a possible related structure model proposed in Ref. 57, the density of the cerium atoms inside reduced ceria remains almost unchanged.

$$\varrho_{\mathrm{rCeria}} = \varrho_{\mathrm{CeO2}} \times \lambda \approx \varrho_{\mathrm{CeO2}} \tag{6}$$

The density of ϱ_{Alloy} can be calculated from the atomic structure model described by the DFT calculation in Ref. 48 (Figure S6b). Overall we obtain:

$$\varrho_{\mathrm{CeO2}} = \varrho_{\mathrm{rCeria}} = \frac{4}{a^2_{\mathrm{CeO2}} \times \sqrt{3}} \tag{7}$$

$$\varrho_{\mathrm{Alloy}} = \frac{1}{a^2_{\mathrm{CePt5}} \times \sin(60°)} \tag{8}$$

For the lattice constant of the oxidized CeO_2 we can take the experimental value ($1.37 \times a_{\mathrm{Pt,lit}} = 5.37$ Å), which we obtained by LEED (see main article). The experimental value for $CePt_5$ can be taken from Ref. 58 ($a_{\mathrm{CePt5}} = 5.37$ Å).

We consider only the reduction step in the second redox cycle (Figure 3e and f and Figure 5 of the main article). With the experimental values of $\sigma_{\mathrm{CeO2}} \approx 70$ % and $\sigma_{\mathrm{rCeria}} \approx 54$ % inserted into Eq. (5) and the densities obtained from Eq. (7) and (8), we obtain the following result: the effective surface coverage of the alloyed support after the reduction covers $\sigma_{\mathrm{rCeria\_alloy}} \approx 63$ % of the entire surface. Since this value would give a surface coverage larger than 100 % ($\sigma_{\mathrm{rCeria}} + \sigma_{\mathrm{rCeria\_alloy}}$), it suggests that a part of the cerium may be used to form more than a monolayer of the alloy, thus involving also deeper layers, or that a Ce richer alloy may be formed in some regions. We discuss this result in more detail in the discussion section (see below).

4.6.2 Model 2

We now consider the case where the uncovered support *of the reduced ceria sample* shall be entirely made from $CePt_5$. As in model 1, we consider one subsurface $CePt_2$ layer of $CePt_5$. As done above for, e.g., Eq. (1), with the percentaged part of the free support $(1 - \sigma_{\mathrm{rCeria}})$ and the density of available cerium sites in the $CePt_5$ alloy (ϱ_{Alloy}), the number of cerium atoms in the alloy is simply given by:

$$N_{\mathrm{Alloy}} = A\,(1 - \sigma_{\mathrm{rCeria}})\,\varrho_{\mathrm{Alloy}} \tag{9}$$

The number of cerium atoms, which get released due to the shrinking ceria islands during the reduction, is equal to $N_{\mathrm{CeO2}} - N_{\mathrm{rCeria}}$ (Eq. (1) and (2), see model 1). As mentioned above, all these atoms shall be incorporated into the uncovered Pt(111) support as a one $CePt_2$ layer. It shall be:

$$N_{\mathrm{CeO2}} - N_{\mathrm{rCeria}} = N_{\mathrm{Alloy}} \tag{10}$$

Note that it is here, where we have a balance: we assume that *all the uncovered support is made from the alloy* after the reduction, because (a) we relate the atom numbers as done in the latter equation and because (b) N_{Alloy} is the number of *all available sites of the uncovered support* (reduced ceria sample), as expressed by Eq. 9. By inserting Eq. (1), (2) and (9) into Eq. (10) we obtain:

$$\sigma_{\mathrm{rCeria}}\,\varrho_{\mathrm{rCeria}} - \sigma_{\mathrm{CeO2}}\,\varrho_{\mathrm{CeO2}} = \frac{(\sigma_{\mathrm{rCeria}} - 1)\;\varrho_{\mathrm{Alloy}}}{2\,\varrho_{\mathrm{CeO2}}}$$

This can be changed to:

$$\sigma_{\mathrm{rCeria}} = \frac{2\,\sigma_{\mathrm{CeO2}}\,\varrho_{\mathrm{CeO2}} - \varrho_{\mathrm{Alloy}}}{2\,\varrho_{\mathrm{rCeria}} - \varrho_{\mathrm{Alloy}}} \tag{11}$$

With help of the densities of cerium in ceria and $CePt_5$ [see Eq. (6) and (7,8)], the surface coverage of the *reduced ceria film* (σ_{rCeria}) can be calculated from σ_{CeO2} and be compared to the experimental value.

As in model 1, we consider only the reduction step in the second redox cycle (Figure 3e and f and Figure 5 of the main article). With the experimental value of $\sigma_{\mathrm{CeO2}} \approx 70$ % inserted into Eq. (11), we obtain the following result: the effective surface coverage of the reduced ceria film is around $\sigma_{\mathrm{rCeria}} \approx 60$ %, i. e., the alloyed uncovered support makes $\sigma_{\mathrm{rCeria\_alloy}} \approx 40$ %. These values are in a good agreement with the experimental values [ceria film: $\sigma_{\mathrm{rCeria}} = (54 \pm 6)$ % $\Rightarrow$ uncovered support: $\sigma_{\mathrm{rCeria\_support}} = (46 \pm 6)$ %, uncovered alloy: $\sigma_{\mathrm{rCeria\_alloy}} = (41 \pm 6)$ %] and support the assumption that the entire uncovered support is made from a one layer thin alloy.

4.6.3 Discussion

Comparison of both models - From *Model 1* and *2* we obtained the following results:

Model	Input		Result	
	σ_{CeO2}	σ_{rCeria}	σ_{rCeria}	$\sigma_{\mathrm{rCeria\_alloy}}$
Model 1	70 %	54 %	N.A.	63 %
Model 2	70 %	N.A.	60 %	40 %

As it can be easily seen, the two values for the coverage $\sigma_{\mathrm{rCeria\_alloy}}$ do not agree, they deviate by 23 %. This makes indeed sense because in *Model 1* the two coverage values (σ_{CeO2} and σ_{rCeria}) do not depend on each other, whereas σ_{rCeria} depends on σ_{CeO2} in *Model 2*. This can be seen by the sum of $\sigma_{\mathrm{rCeria\_alloy}}$ and σ_{rCeria}, which is by definition a 100 % in *Model 2* and 117 % in *Model 1*.

All the latter will be further analyzed with the help of Figure S7, where σ_{rCeria} as a function of σ_{CeO2} (blue line) is shown (*Model 2*). The gray dotted lines show the point on the curve, which belongs to the pair σ_{CeO2} = 70 % / σ_{rCeria} = 60 % obtained in *Model 2*. The light blue square symbolizes the error of both ($\pm$6 %). Now we consider the pair σ_{CeO2} = 70 % / σ_{rCeria} = 54 % used as an input in *Model 1*: the light blue horizontal line shows the place of σ_{rCeria} = 54 % on the blue curve obtained by *Model 2*, with a light blue square for its error. The light blue vertical line shows that *Model 1* had yielded indeed the same result as *Model 2*, if the coverage of the oxidized ceria film would have been experimentally determined to be σ_{CeO2} = 65.5 % and not 70 %.

If the errors symbolized by the light blue squares in Figure S7 are considered, an overlap can be seen (small square in dark blue color). The small square shows that it is justified to assume that within our experimental error of 6 %, the values for σ_{CeO2} and σ_{rCeria} in this small region correspond to the case where *Model 1* is in agreement with *Model 2*.

Predictions from *Model 2* - A very interesting result is represented by the green curve (*Model 2*), which shows the change of the surface coverage of ceria film upon reduction ($\triangle\sigma = \sigma_{\mathrm{CeO2}} - \sigma_{\mathrm{rCeria}}$): when the coverage σ_{CeO2} of the oxidized film is around 100 % of the surface, the shrinking of the film is close to zero ($\triangle\sigma \approx 0$) because the coverage of the reduced ceria film is almost the same ($\sigma_{\mathrm{rCeria}} \approx \sigma_{\mathrm{CeO2}}$). This makes sense because no free area of the support can be used to form the alloy. However, towards smaller coverages σ_{CeO2}, the relative change $\triangle\sigma$ increases, up to the point ($\sigma_{\mathrm{CeO2}} \approx 25$ %, see vertical yellow dotted line) where all the ceria is consumed during reduction for the formation of an alloy ($\sigma_{\mathrm{rCeria}} \approx 0$ at blue line: no ceria film after reduction). Experiments must clarify in future, if this prediction is indeed valid.

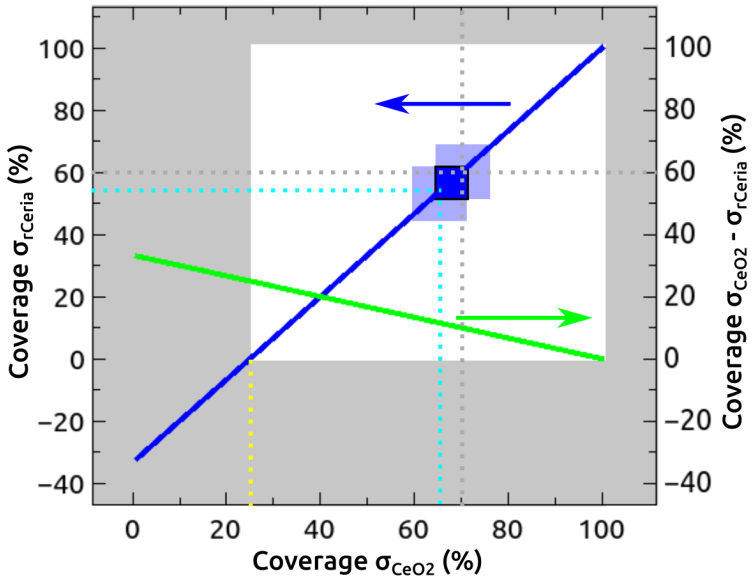

Figure S7: Results of *Model 2*. The blue curve represents the surface coverage of the reduced ceria film (σ_{rCeria}) as a function of the coverage of the oxidized film (σ_{CeO2}). The model is only valid in the white but not in the gray shaded regions. The gray dotted vertical and horizontal lines mark the experimental value for $\sigma_{\mathrm{CeO2}} = 70$ % and the resulting value for $\sigma_{\mathrm{rCeria}} = 60$ %. The green curve shows the relative change of the coverage $\triangle\sigma = \sigma_{\mathrm{CeO2}} - \sigma_{\mathrm{rCeria}}$ as a function of σ_{CeO2}. More details can be found in the text.

References

(1) Luches, P.; Pagliuca, F.; Valeri, S. Morphology, Stoichiometry, and Interface Structure of CeO_2 Ultrathin Films on Pt(111). *J. Phys. Chem. C* **2011**, *115*, 10718–10726.

(2) Barth, C.; Claeys, C.; Henry, C. R. Surface Preparation of Hard Ionic Crystals by Ultrahigh Vacuum Cleavage. *Rev. Sci. Instr.* **2005**, *76*, 083907.

(3) Lubuntu, Canonical (London, UK) (2018).

(4) Barth, C. X11 Forwarding, How to Change Strange Colors? (2016).

(5) The Gwyddion Open Source Project (2018).

(6) The Matplotlib Open Source Project (2018)

(7) The Python Open Source Project (2018)

(8) Albrecht, T. R.; Grütter, P.; Horne, D.; Rugar, D. Frequency Modulation Detection Using High-Q Cantilevers for Enhanced Force Microscope Sensitivity. *J. Appl. Phys.* **1991**, *69*, 668.

(9) Kitamura, S.; Suzuki, K.; Iwatsuki, M. High Resolution Imaging of Contact Potential Difference Using a

Novel Ultrahigh Vacuum Non-Contact Atomic Force Microscope Technique. *Appl. Surf. Sci.* **1999**, *140*, 265–270.

(10) Palacios-Lidon, E.; Henry, C. R.; Barth, C. Kelvin Probe Force Microscopy in Surface Chemistry: Reactivity of Pd Nanoparticles on Highly Oriented Pirolytic Graphite. *ACS Catal.* **2014**, *4*, 1838–1844.

(11) Skála, T.; Sutara, F.; Prince, K. C.; Matolín, V. Cerium Oxide Stoichiometry Alteration via Sn Deposition: Influence of Temperature. *J. Electron. Spectrosc. Relat. Phenom.* **2009**, *169*, 20–25.

(12) Skála, T.; Sutara, F.; Skoda, M.; Prince, K. C.; Matolín, V. Palladium Interaction with CeO_2, Sn-Ce-O and Ga-Ce-O Layers. *J. Phys. Condens. Matter* **2009**, *21*, 055005.

(13) Gangopadhyay, S.; Frolov, D. D.; Masunov, A. E.; Seal, S. Structure and Properties of Cerium Oxides in Bulk and Nanoparticulate Forms. *J. Alloys Compd.* **2014**, *584*, 199–208.

(14) Hull, A. W. X-Ray Crystal Analysis of Thirteen Common Metals. *Phys. Rev.* **1921**, *17*, 571–588.

(15) Uspenski, N.; Konobejewski, S. Die Beugung der Röntgenstrahlen in Mikrokristallinischen Strukturen. *Zeitschrift Phys.* **1923**, *16*, 215–227.

(16) Davey, W. P. Precision Measurements of the Lattice Constants of Twelve Common Metals. *Phys. Rev.* **1925**, *25*, 753.

(17) Barth, T.; Lunde, G. Die Gitterkonstanten des Platinmetalle, Silber und Gold. *Zeitschrift Phys. Chem.* **1926**, *121*, 78–102.

(18) Bredig, G.; Allolio, R. Röntgenuntersuchungen an Katalytisch Wirkenden Metallen. *Zeitschrift Phys. Chem.* **1927**, *126*, 41–71.

(19) Owen, E. A.; Yates, E. L. XLI. Precision Measurements of Crystal Parameters. *The London, Edinburgh, and Dublin Philosophical Magazine and Journal of Science* **1933**, *15*, 472–488.

(20) Edwards, J. W.; Speiser, R.; Johnston, H. L. High Temperature Structure and Thermal Expansion of Some Metals as Determined by X-Ray Diffraction Data. I. Platinum, Tantalum, Niobium, and Molybdenum. *J. Appl. Phys.* **1951**, *22*, 424–428.

(21) Ellner, M. Zusammenhang zwischen Strukturellen und Thermo-Dynamischen Eigenschaften bei Phasen der Kupfer-Familie in T^{10}-B^4-Systemen. *J. Less Common Met.* **1981**, *78*, 21–32.

(22) Eichler, A.; Mittendorfer, F.; Hafner, J. Precursor-Mediated Adsorption of Oxygen on the (111) Surfaces of Platinum-Group Metals. *Phys. Rev. B* **2000**, *62*, 4744–4755.

(23) Ample, F.; Clotet, A.; Ricart, J. M. Structure and Bonding Mechanism of Cyanide Adsorbed on Pt(111). *Surf. Sci.* **2004**, *558*, 111–121.

(24) Da Silva, J. L. F.; Stampfl, C.; Scheffler, M. Converged Properties of Clean Metal Surfaces by All-Electron First-Principles Calculations. *Surf. Sci.* **2006**, *600*, 703–715.

(25) Haas, Ph.; Tran, F.; Blaha, P. Calculation of the Lattice Constant of Solids with Semilocal Functionals. *Phys. Rev. B* **2009**, *79*, 085104.

(26) Pang, Q.; Zhang, Y.; Zhang, J.; Xu, K. Structural and Electronic Properties of Atomic Oxygen Adsorption on Pt(111): A Density-Functional Theory Study. *Appl. Surf. Sci.* **2011**, *257*, 3047–3054.

(27) Clay, J. P.; Greeley, J. P.; Ribeiro, F. H.; Nicholas Delgass, W.; Schneider, W. F. DFT Comparison of Intrinsic WGS Kinetics over Pd and Pt. *J. Catal.* **2014**, *320*, 106–117.

(28) Patra, A.; Bates, J. E.; Sun, J.; Perdew, J. P. Properties of Real Metallic Surfaces: Effects of Density Functional Semilocality and Van der Waals Nonlocality. *Proc. Natl. Acad. Sci.* **2017**, *114*, E9188–E9196.

(29) Brauer, G.; Gingerich, K. A. Über die Oxyde des Cers-V: Hochtemperatur-Röntgenuntersuchungen an Ceroxyden. *J. Inorg. Nucl. Chem.* **1960**, *16*, 87–99.

(30) Duclos, S. J.; Vohra, Y. K.; Ruoff, A. L.; Jayaraman, A.; Espinosa, G. P. High-Pressure X-Ray Diffraction Study of CeO_2 to 70 GPa and Pressure-Induced Phase Transformation from the Fluorite Structure. *Phys. Rev. B* **1988**, *38*, 7755–7758.

(31) Gerward, L.; Staun Olsen, J. Powder Diffraction Analysis of Cerium Dioxide at High Pressure. *Powder Diff.* **1993**, *8*, 127–129.

(32) Rossignol, S.; Gérard, F.; Mesnard, D.; Kappenstein, Ch.; Duprez, D. Structural Changes of Ce-Pr-O Oxides in Hydrogen: a Study by In-Situ X-Ray Diffraction and Raman Spectroscopy. *J. Mater. Chem.* **2003**, *13*, 3017–3020.

(33) Gerward, L.; Staun Olsen, J.; Petit, L.; Vaitheeswaran, G.; Kanchana, V.; Svane, A. Bulk Modulus of CeO_2 and PrO_2 - An Experimental and Theoretical Study. *J. Alloys Compd.* **2005**, *400*, 56–61.

(34) Marien, J. *Bull. Soc. R. Sci. Liege* **1976**, *45*, 103.

(35) Nieuwenhuys, B. E. Influence of the Surface Structure on the Adsorption of Hydrogen on Platinum, as Studied by Field Emission Probe-Hole Microscopy. *Surf. Sci.* **1976**, *59*, 430–446.

(36) Demuth, J. E. Ultraviolet Photoemission Studies of Hydrogen Chemisorption Bonding to Ni, Pd and Pt Surfaces. *Surf. Sci.* **1977**, *65*, 369–375.

(37) Collins, D. M.; Spicer, W. E. The Adsorption of CO, O_2, and H_2 on Pt. *Surf. Sci.* **1977**, *69*, 114–132.

(38) Fisher, G. B. The Electronic Structure of two Forms of Molecular Ammonia Adsorbed on Pt(111). *Chem. Phys. Lett.* **1981**, *79*, 452–458.

(39) Salmerón, M.; Ferrer, S.; Jazzar, M.; Somorjai, G. A. Photoelectron-Spectroscopy Study of the Electronic Structure of Au and Ag Overlayers on Pt(100), Pt(111), and Pt(997) Surfaces. *Phys. Rev. B* **1983**, *28*, 6758–6765.

(40) Kiskinova, M.; Pirug, G.; Bonzel, H. P. Coadsorption of Potassium and CO on Pt(111). *Surf. Sci.* **1983**, *133*, 321–343.

(41) Fargues, D.; Ehrhardt, J. J.; Abon, M.; Bertolini, J. C. Photoemission of Adsorbed Xenon on Pt_xNi_{1-x}(111) Single Crystal Alloy Surfaces. *Surf. Sci.* **1988**, *194*, 149–158.

(42) Alnot, M.; Ehrhardt, J. J.; Barnard, J. A. A Characterization of Heterogeneous Pt Surfaces by Work Function Measurements and Photoemission of Adsorbed Xenon. *Surf. Sci.* **1989**, *208*, 285–305.

(43) Derry, G. N.; Ji-Zhong, Z. Work Function of Pt(111). *Phys. Rev. B* **1989**, *39*, 1940–1941.

(44) Cousty, J.; Papageorgopoulos, C. A.; Riwan, R. Electronic Properties of Cs Layers Adsorbed on Pt(111). *Surf. Sci.* **1989**, *223*, 479–492.

(45) Ranke, W.; Weiss, W. Photoemission of Ethylbenzene Adsorbed on Pt(111) and on Epitaxial Films of FeO(111) and Fe_3O_4(111): Electronic Structure and Isosteric Heats of Adsorption. *Surf. Sci.* **1998**, *414*, 236–253.

(46) Singh-Miller, N. E.; Marzari, N. Surface Energies, Work Functions, and Surface Relaxations of Low-Index Metallic Surfaces from First Principles. *Phys. Rev. B* **2009**, *80*, 235407.

(47) Khomyakov, P. A.; Giovannetti, G.; Rusu, P. C.; Brocks, G.; van den Brink, J.; Kelly, P. J. First-Principles Study of the Interaction and Charge Transfer between Graphene and Metals. *Phys. Rev. B* **2009**, *79*, 235407.

(48) Tereshchuk, P.; Piotrowski, M. J.; Da Silva, J. L. F. Atomic Structure of the La/Pt(111) and Ce/Pt(111) Surfaces Revealed by DFT+U Calculations. *RSC Adv.* **2015**, *5*, 521–528.

(49) Derry, G. N.; Kern, M. E.; Worth, E. H. Recommended Values of Clean Metal Surface Work Functions. *J. Vac. Sci. Technol. A* **2015**, *33*, 060801.

(50) Mullins, D. R.; Overbury, S. H.; Huntley, D. R. Electron Spectroscopy of Single Crystal and Polycrystalline Cerium Oxide Surfaces. *Surf. Sci.* **1998**, *409*, 307–319.

(51) Hasegawa, T.; Shahed, S. M. F.; Sainoo, Y.; Beniya, A.; Isomura, N.; Watanabe, Y.; Komeda, T. Epitaxial Growth of CeO_2(111) Film on Ru(0001): Scanning Tunneling Microscopy (STM) and X-Ray Photoemission Spectroscopy (XPS) Study. *J. Chem. Phys.* **2014**, *140*, 044711.

(52) Kundakovic, L.; Mullins, D. R.; Overbury, S. H. Adsorption and Reaction of H_2O and CO on Oxidized and Reduced Rh/CeO_x(111) Surfaces. *Surf. Sci.* **2000**, *457*, 51–62.

(53) Henderson, M. A.; Perkins, C. L.; Engelhard, M. H.; Thevuthasan, S.; Peden, C. H. F. Redox Properties of Water on the Oxidized and Reduced Surfaces of CeO_2(111). *Surf. Sci.* **2003**, *526*, 1–18.

(54) Sadewasser, S.; Lux-Steiner, M. C. Correct Height Measurement in Noncontact Atomic Force Microscopy. *Phys. Rev. Lett.* **2003**, *91*, 266101.

(55) Terris, B. D.; Stern, J. E.; Rugar, D.; Mamin, H. J. Localized Charge Force Microscopy. *J. Vac. Sci. Technol. A* **1990**, *8*, 374–377.

(56) Barth, C.; Hynninen, T.; Bieletzki, M.; Henry, C. R.; Foster, A. S.; Esch, F.; Heiz, U. AFM Tip Characterization by Kelvin Probe Force Microscopy. *New J. Phys.* **2010**, *12*, 093024.

(57) Duchon, T.; Dvorak, F.; Aulická, M.; Stetsovych, V.; Vorokhta, M.; Mazur, D.; Veltruská, K.; Skala, T.; Myslivecek, J.; Matolínová, I. et al. Ordered Phases of Reduced Ceria as Epitaxial Films on Cu(111). *J. Phys. Chem. C* **2013**, *118*, 357–365.

(58) Adroja, D. T.; Malik, S. K.; Padalia, B. D.; Vijayaraghavan, R. Structural and Magnetic Studies on $CeTPt_4$ (T=Cu, Ga, Rh, Pd, and In) Compounds. *Solid State Commun.* **1989**, *71*, 649–651.